

the following frequencies: 628.59, 662.86, 1040.64, 1117.90, 1316.0, 1416.22, 1792.32, 3083.01, and 3749.88  $\text{cm}^{-1}$ . The two lowest frequencies correspond to the torsional angles of the OH and CH bonds, respectively.

For the two lower singlet states,  $S_0$  and  $S_1$ , we calculate a two-dimensional grid composed of 37 equally spaced points for  $\phi_1$  and  $\phi_2$ , fixing the rest of coordinates to the corresponding values listed in Table A.1. These points are interpolated using a two-dimension splines method to get the potential energy surfaces,  $S_0$  and  $S_1$ , at any desired geometry, including the two conformers.

The potential energy surface of the  $S_0$  electronic state presents two minima for  $\phi_2 = 0^\circ$ , one at  $\phi_1 = 0^\circ$  or  $360^\circ$  (*trans*), and a second at  $\phi_1 = 180^\circ$  (*cis*). As illustrated in Fig. A.1, both minima correspond to a planar geometry. The potential for the  $S_1$  excited state presents two equivalent wells for the *trans*-conformer ( $\phi_1 = 300^\circ$ ,  $\phi_2 = 120^\circ$  or  $\phi_1 = 60^\circ$ ,  $\phi_2 = 240^\circ$ ). Therefore, the minimum geometrical configuration in the  $S_1$  excited state is no longer planar. The *cis* conformer minimum transforms into a shoulder of the potential. This is shown in the one-dimensional cut shown in Fig. A.1 for the case of  $\phi_2 = 120^\circ$ . In this case, the potential energy surface as a function of  $\phi_1$  is rather flat, while it shows a double-well structure as a function of  $\phi_2$ , corresponding to geometries above and below the molecular plane.

**Table A.1.** Optimized geometries for *trans*-HCOOH in the ground ( $S_0$ ) and excited electronic state ( $S_1$ ). Distances are in Angstrom and angles in degree units.

Geometry of <i>trans</i> -HCOOH	$S_0$ ground-state (geom- $S_0$ )	$S_1$ excited-state (geom- $S_1$ )
R(CO <sub>1</sub> )	1.1987	1.3683
R(CO <sub>2</sub> )	1.3600	1.3840
$\theta$ (O <sub>1</sub> CO <sub>2</sub> )	122.38	111.17
R(CH <sub>1</sub> )	1.1008	1.0751
$\theta$ (O <sub>1</sub> CH <sub>1</sub> )	124.01	113.06
R(OH <sub>1</sub> )	0.9663	0.9661
$\theta$ (CO <sub>2</sub> H <sub>2</sub> )	108.72	107.51
$\phi_1$ (H <sub>2</sub> O <sub>2</sub> CO <sub>1</sub> )	0.00	55.32
$\phi_2$ (H <sub>1</sub> CO <sub>1</sub> O <sub>2</sub> )	180.00	232.28

## Appendix A: *Ab initio* estimation of fluorescence cross-sections and photoisomerization probabilities

In this appendix, we demonstrate that the detected *cis*-HCOOH towards the Orion Bar can be produced by a gas-phase photo-switching mechanism. To estimate the FUV photon absorption cross-sections and probabilities of the *trans-cis* photoisomerization process, we start calculating the potential energy surfaces of the HCOOH  $S_0$  and  $S_1$  electronic states as a function of the two most relevant degrees of freedom, the torsional angle of OH ( $\phi_1$ ), and the torsional angle of CH ( $\phi_2$ ) (see Fig. A.1).

We performed ic-MRCI-F12 *ab initio* calculations using the MOLPRO suite of programs<sup>1</sup> with the VDZ-F12 basis set. The obtained results agree with the stationary points previously reported by Maeda et al. (2012, 2015). The molecular orbitals and reference configurations were determined with a CASSCF calculation using 16 active orbitals. The optimized equilibrium geometries in the  $S_0$  and  $S_1$  electronic states are in agreement with previous results, corresponding to planar and bent *trans*-HCOOH conformers, respectively. They are listed in Table A.1. For *trans*-HCOOH, the normal modes in the  $S_0$  state have

<sup>1</sup> MOLPRO (Werner et al. 2012), version 2012, is a package of *ab initio* programs for advanced molecular electronic structure calculations, designed and maintained by H.-J. Werner and P. J. Knowles, and with contributions from many other authors (see <http://www.molpro.net>).

We solved the two-dimension Shrödinger equation for  $\phi_1$  and  $\phi_2$  and obtained the vibrational eigenfunctions. The first six vibrational levels of the  $S_0$  electronic state correspond to the *trans* conformer, the seventh energy level corresponds to the ground-vibrational state of *cis*-HCOOH. In the  $S_1$  excited electronic state, the presence of a double well as a function of  $\phi_2$  implies that two degenerate vibrational states appear. The two well depths are different in geom- $S_0$  and geom- $S_1$  which means that their nodal structure significantly changes.

In a second step, we calculate the transition dipole moments for the two-dimensional grids of geom- $S_0$  and geom- $S_1$ , and determine the transitions between the  $S_0$  state and the  $S_1$  state. We derive the absorption spectra starting from both *trans*-HCOOH ( $\nu = 0$ ) and *cis*-HCOOH ( $\nu = 7$ ) in the  $S_0$  electronic ground-state, to the first 200 vibrational levels of the  $S_1$  excited-state. The use of different geometries in the two electronic states allows us to approximately reproduce the experi-

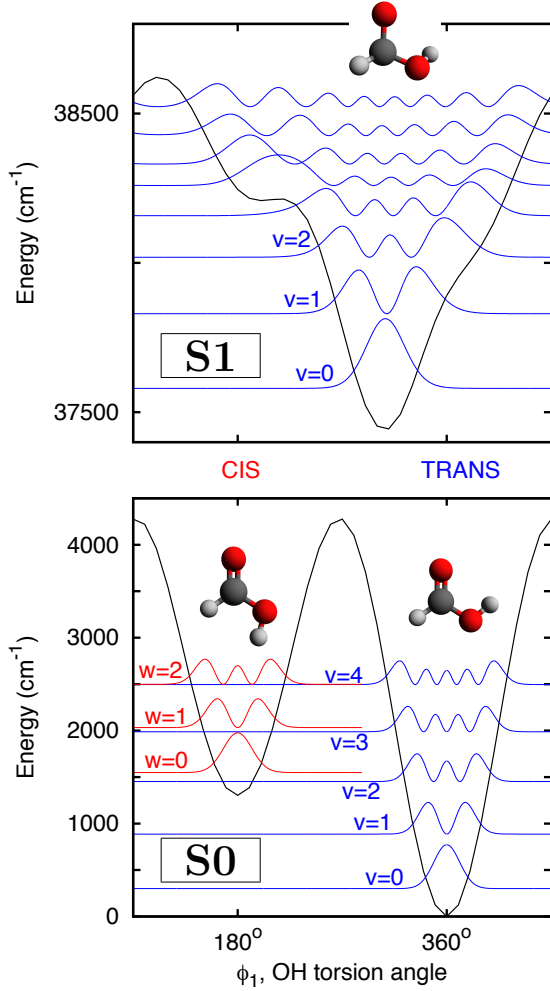


**Fig. A.1.** One-dimensional potential energy surfaces of HCOOH as function of the OH torsional angle  $\phi_1$ . *Bottom panel:* ground  $S_0$  electronic state. *Top panel:* excited  $S_1$  state. One-dimensional cuts were obtained from the two-dimensional grid (see text) by setting  $\phi_2 = 180^\circ$  and  $\phi_2 = 300^\circ$  for  $S_0$  and  $S_1$ , respectively. We also show the vibrational-wave functions obtained from a one-dimensional model. The different geometrical structures of the HCOOH molecule in each energy minimum are shown.

mental frequencies (Beatty-Travis et al. 2002). The absorption spectrum is obtained using the transition dipole moments obtained for geom- $S_0$ .

The calculated radiative lifetimes of the different vibrational levels of the  $S_1$  electronic excited-state vary from  $75 \times 10^{-6}$  s to  $375 \times 10^{-6}$  s, but each level has a different probability to decay towards the *trans* of *cis* well of the  $S_0$  ground electronic state. We explicitly determine the probability to fluoresce into each conformer by calculating:

$$P_{cis(\nu)} = \sum_{\nu', cis} \left| \langle f_{\nu'}^{S_0} | d | f_{\nu}^{S_1} \rangle \right|^2 \quad (\text{A.1})$$

and

$$P_{trans(\nu)} = \sum_{\nu', trans} \left| \langle f_{\nu'}^{S_0} | d | f_{\nu}^{S_1} \rangle \right|^2 \quad (\text{A.2})$$

where we separate the contributions of the  $\nu'$  levels corresponding to the *trans* or *cis* conformers and normalize the sum to 1. We then normalize the above values and compute  $P_{cis(\nu)}/(P_{cis(\nu)}+P_{trans(\nu)})$  and  $P_{trans(\nu)}/(P_{cis(\nu)}+P_{trans(\nu)})$

for  $\nu$  levels corresponding to absorption energies below about  $40000 \text{ cm}^{-1}$  ( $E < 5 \text{ eV}$ ), approximately the energy for which the dominant photodissociation channel opens and fluorescence starts to become negligible.

In summary, with these *ab initio* calculations we estimate the *cis*- and *trans*-HCOOH cross-sections  $\sigma_{\lambda_i}$  for absorption of photons with energies lower than about  $40000 \text{ cm}^{-1}$  (those producing fluorescence). These absorptions radiatively excite the molecule to the  $S_1$  electronic excited-state. We explicitly compute the  $\sigma_{\lambda_i}$  values for each photon energy as well as the probabilities to fluoresce back to a specific *cis* or *trans* state (i.e. we determine the normalized probabilities of the different *trans*  $\rightarrow$  *cis*, *trans*  $\rightarrow$  *trans*, *cis*  $\rightarrow$  *cis*, *cis*  $\rightarrow$  *trans* bound-bound transitions). The  $\sigma_{\lambda_i}(\text{trans})$  and  $\sigma_{\lambda_i}(\text{cis})$  cross-sections and the  $P_{trans \rightarrow cis}$  and  $P_{cis \rightarrow trans}$  probabilities are plotted in Fig. 3.

## Appendix B: Estimation of the photoisomerization rate in the Orion Bar

The number of photoisomerizations per second depends on the flux of FUV photons with energies below 5 eV. The *trans*-to-*cis* and *cis*-to-*trans* photoisomerization rates ( $\xi_{tc}$  and  $\xi_{ct}$ ) are derived from the discrete sums:

$$\xi_{tc} = \sum_{\lambda_i} N_{\text{ph}, \lambda_i} \cdot \sigma_{\lambda_i}(\text{trans}) \cdot P_{t \rightarrow c} \quad (\text{B.1})$$

and

$$\xi_{ct} = \sum_{\lambda_i} N_{\text{ph}, \lambda_i} \cdot \sigma_{\lambda_i}(\text{cis}) \cdot P_{c \rightarrow t} \quad (\text{B.2})$$

where  $\sigma_{\lambda_i}$  is the absorption cross-section from a given conformer (in  $\text{cm}^2 \text{ photon}^{-1}$ ) and  $P$  is the probability to fluoresce from one isomer to the other. Both quantities are determined from our *ab initio* calculations (previous section).  $N_{\text{ph}, \lambda_i}$  (photon  $\text{cm}^{-2} \text{ s}^{-1}$ ) is the flux of photons at each wavelength producing absorption.

In order to estimate the most realistic  $\xi_{tc}$  and  $\xi_{ct}$  rates for the FUV-irradiation conditions in the Orion Bar, we used the Meudon PDR code (Le Petit et al. 2006) and calculate  $N_{\text{ph}}(\lambda)$  at different cloud depth  $A_V$  values. Following our previous studies of the Bar (Cuadrado et al. 2015; Goicoechea et al. 2016) we run a model of an isobaric PDR ( $P_{\text{th}}/k = 10^8 \text{ K cm}^{-3}$ ) illuminated by  $\chi = 4 \times 10^4$  times the mean interstellar radiation field (Draine 1978). For photons in the  $\lambda = 2000 - 3000 \text{ \AA}$  range, we adopt  $N_{\text{ph}}(\lambda) = 4 \times 10^4 \times 732 \times \lambda^{0.7} \text{ photon cm}^{-2} \text{ s}^{-1} \text{ \AA}^{-1}$  at the PDR edge ( $A_V = 0$ ) (van Dishoeck & Black 1982). We use a constant dust composition and size distribution that reproduces standard interstellar extinction curve (Cardelli et al. 1989).

Table B.1 shows the resulting photoisomerization rates at different cloud depths, the expected *trans*-to-*cis* HCOOH abundance ratio at equilibrium, and the time needed to reach the equilibrium ratios (neglecting photodissociation).

The use of constant dust grain properties through the PDR is likely the most important simplification for the calculation of the photoisomerization rates  $\xi_{tc}$  and  $\xi_{ct}$ . Grain populations are known to evolve in molecular clouds, especially in PDRs where the sharp attenuation of a strong FUV field results in a stratification of the dust and PAH properties with  $A_V$  (Draine 2003). Therefore, although the varying optical properties of grains are difficult to quantify and include in PDR models, they likely play a role on how FUV photons of different energies are differentially absorbed as a function of  $A_V$  (Goicoechea & Le Boulrot 2007). For the particular case of HCOOH, the strength and width of the  $2175 \text{ \AA}$  extinction bump (Cardelli et al. 1989) naturally

**Table B.1.** Photoisomerization rates for the irradiation conditions in the Orion Bar.

Cloud depth $A_V$ [mag]	$N_{\text{ph}}$ (2300 – 2800 Å) [photons $\text{cm}^{-2} \text{s}^{-1}$ ]	$\xi_{\text{ic}}$ [ $\text{s}^{-1}$ ]	$\xi_{\text{ct}}$ [ $\text{s}^{-1}$ ]	<i>trans/cis</i> -HCOOH ratio at equilibrium	Time [years]
0	$1.96 \times 10^{12}$	$5.45 \times 10^{-11}$	$1.27 \times 10^{-10}$	2.3	$1.7 \times 10^2$
1	$1.80 \times 10^{11}$	$3.41 \times 10^{-12}$	$9.89 \times 10^{-12}$	2.9	$2.4 \times 10^3$
2	$2.84 \times 10^{10}$	$3.79 \times 10^{-13}$	$1.31 \times 10^{-12}$	3.5	$1.9 \times 10^4$
3	$4.93 \times 10^9$	$4.62 \times 10^{-14}$	$1.87 \times 10^{-13}$	4.1	$1.3 \times 10^5$
5	$1.69 \times 10^8$	$7.83 \times 10^{-16}$	$4.29 \times 10^{-15}$	5.5	$6.2 \times 10^6$

divides the range of photons producing HCOOH photodissociation (those with  $E > 5$  eV) from those producing fluorescence ( $E < 5$  eV). The extinction bump has been related with the absorption of FUV photons by PAH mixtures and small carbonaceous grains (Joblin et al. 1992; Draine 2003). Although it is not known how the bump evolves with  $A_V$ , it clearly determines how the lower-energy FUV photons are absorbed. In Fig. 3 (bottom panel) we show different extinction curves for different PAH abundances (Goicoechea & Le Bourlot 2007). Optical properties are taken from Li & Draine (2001) and references therein. In addition, and as in most PDR models, our predicted FUV spectrum does not include the absorption produced by hundreds of molecular electronic transitions blanketing the FUV spectrum (other than  $\text{H}_2$  and CO lines). All together, our assumption that the detected *cis*-HCOOH arises from PDR layers in which the flux of photons with  $\lambda > 2500$  Å dominates over the higher-energy photodissociating photons is very plausible.

### Appendix C: Alternative mechanisms for *trans*-to-*cis* isomerization in the ISM

Searching for further support to the photoswitching scenario, we qualitatively explored other possibilities that may apply in interstellar conditions. In the laboratory, *trans*-to-*cis* isomerization has been observed in molecular ices irradiated by near-IR photons (Maçôas et al. 2004; Olbert-Majkut et al. 2008). Hence, isomerization of solid HCOOH and subsequent desorption to the gas-phase might also be responsible of the *cis*-HCOOH enhancement. However, owing to the short lifetime of the *cis* conformer observed in ices (a few minutes if the irradiation is stopped, Maçôas et al. 2004), a very strong flux of IR photons would be needed to maintain significant abundances of solid *cis*-HCOOH. In addition, near-IR photons penetrate molecular clouds much deeper than FUV photons, and one would have expected to detect *cis*-HCOOH in all positions of the Bar, and towards the Orion hot core, a region irradiated by intense IR fields. Alternatively, the *trans*-to-*cis* isomerization might be triggered by collisions with electrons. Electrons are relatively abundant in FUV-irradiated environments (with ionisation fractions up to about  $n_e/n_{\text{H}} \approx 10^{-4}$ ) compared to shielded cloud interiors ( $n_e/n_{\text{H}} \approx 10^{-9}$ ). Simple calculations show that electrons with energies of about 0.5 eV would be needed to overcome the energy barrier to HCOOH isomerization, and to produce a *trans*-to-*cis* abundance ratio of about 3. Such suprathermal electrons could be provided by the photoionisation of low ionisation potential atoms (C, S, Si...), but their abundance sharply decrease with  $A_V$  (Hollenbach & Tielens 1999). We estimate that at a cloud depth of  $A_V = 2$  mag, HCOOH collisional isomerization, if effective, could compete with photoswitching only if the elastic collisional rate coefficients were very high, of the order of

$>10^{-6} \text{ cm}^3 \text{ s}^{-1}$  for a typical electron density of  $n_e < 1 \text{ cm}^{-3}$  in PDRs. However, the detection of *trans*-HCOOH, but not *cis*-HCOOH, towards other PDRs such as the Horsehead (Guzmán et al. 2014), with similar electron densities but much lower FUV photon flux ( $>100$  times less than the Bar), supports a photoswitching mechanism in the Orion Bar (i.e. high  $\xi_{\text{ic}}$  and  $\xi_{\text{ct}}$  rates), but makes it too slow for the Horsehead and other low FUV-flux sources. Either way, we encourage laboratory and theoretical studies of the possible role of electron collisions, as well as of a more detailed investigation of the HCOOH, and other species, photoswitching mechanism.

### Appendix D: Rotational diagrams and column density calculation

Owing to the large number of detected HCOOH lines, we calculated rotational temperatures ( $T_{\text{rot}}$ ) and column densities ( $N$ ) from rotational population diagrams. The standard relation for the rotational diagram (Goldsmith & Langer 1999) is:

$$\ln \frac{N_u}{g_u} = \ln N - \ln Q_{\text{rot}} - \frac{E_u}{kT_{\text{rot}}}, \quad (\text{D.1})$$

with  $N_u/g_u$  given by

$$\frac{N_u}{g_u} = \frac{8\pi k}{h c^3} \cdot \frac{\nu_{ul}^2}{A_{ul} g_u} \cdot \eta_{\text{bf}}^{-1} \cdot \int T_{\text{MB}} dv \quad [\text{cm}^{-2}], \quad (\text{D.2})$$

In the above relation,  $N_u$  is the column density of the upper level in the optically thin limit [ $\text{cm}^{-2}$ ],  $N$  is the total column density [ $\text{cm}^{-2}$ ],  $g_u$  is the statistical weight of the upper state of each level,  $Q_{\text{rot}}$  is the rotational partition function evaluated at a rotational temperature  $T_{\text{rot}}$ ,  $A_{ul}$  is the Einstein coefficient [ $\text{s}^{-1}$ ],  $E_u/k$  is the energy of the upper level of the transition [K],  $\nu_{ul}$  is the frequency of the  $u \rightarrow l$  transition [ $\text{s}^{-1}$ ],  $\int T_{\text{MB}} dv$  is the velocity-integrated line intensity corrected from beam efficiency [ $\text{K km s}^{-1}$ ], and  $\eta_{\text{bf}}$  is the beam filling factor. Assuming that the emission source has a 2D Gaussian shape,  $\eta_{\text{bf}}$  is equal to  $\eta_{\text{bf}} = \theta_S^2 / (\theta_S^2 + \theta_B^2)$ , with  $\theta_B$  the HPBW of the telescope [arcsec] and  $\theta_S$  the diameter of the Gaussian source [arcsec]. The values for  $\nu_{ul}$ ,  $E_u/k$ ,  $g_u$ , and  $A_{ul}$  are taken from the MADEX spectral catalogue.

Rotational diagrams were built considering two limiting cases: (i) that the detected HCOOH emission is extended, with  $\eta_{\text{bf}} = 1$ ; and (ii) that the emission is semi-extended, with  $\theta_S = 9''$  (Cuadrado et al. 2015). In a plot of  $\ln(N_u/g_u)$  versus the energy of the upper level of each rotational transition,  $E_u/k$ , the population distribution roughly follows a straight line with a slope  $-1/T_{\text{rot}}$ . The total column density of the molecule,  $N$ , is obtained from the  $y$ -intercept and the partition function. Figure C.1 shows

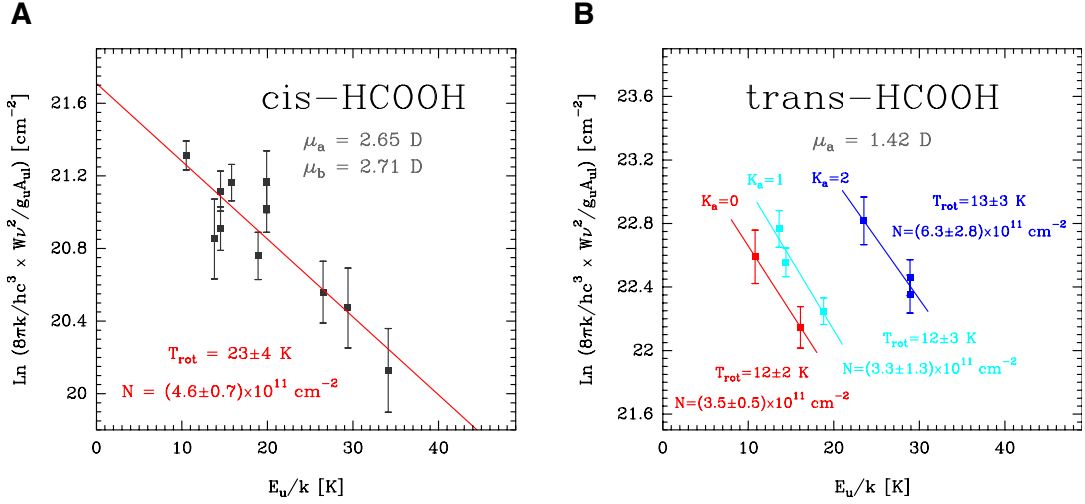


**Fig. C.1.** Rotational population diagrams from the observed HCOOH lines towards the Orion Bar, (+10′, -10′) position. *Left:* Diagram for the *cis* conformer (measurements lie along a single component). *Right:* Diagram for the *trans* conformer showing how different  $K_a$  rotational ladders split in different components. Fitted values of the rotational temperature,  $T_{\text{rot}}$ , and column density,  $N$ , are indicated in each panel (see also Table C.1).

**Table C.1.** Rotational temperatures ( $T_{\text{rot}}$ ), column densities ( $N$ ), and abundances towards the Orion Bar PDR, (+10′, -10′) position.

	Extended source		Semi-extended source		Abundance*	Notes
	$T_{\text{rot}}$ [K]	$N(X)$ [cm <sup>-2</sup> ]	$T_{\text{rot}}$ [K]	$N(X)$ [cm <sup>-2</sup> ]		
<i>cis</i> -HCOOH	23 (4)	$4.6 (0.7) \times 10^{11}$	21 (4)	$4.2 (0.6) \times 10^{12}$		a
<i>trans</i> -HCOOH $K_a = 0$	12 (2)	$3.5 (0.5) \times 10^{11}$	6 (1)	$4.1 (0.6) \times 10^{12}$		a, b
<i>trans</i> -HCOOH $K_a = 1$	12 (3)	$3.3 (1.3) \times 10^{11}$	6 (1)	$3.6 (2.1) \times 10^{12}$		a
<i>trans</i> -HCOOH $K_a = 2$	13 (3)	$6.3 (2.8) \times 10^{11}$	7 (1)	$5.0 (2.4) \times 10^{12}$		a
<b>[(<i>cis</i>+<i>trans</i>)-HCOOH]</b>	—	$1.8 (0.3) \times 10^{12}$	—	$1.7 (0.3) \times 10^{13}$	$(0.3 - 2.7) \times 10^{-10}$	c

**Notes.** \* The abundance of each species with respect to H nuclei is given by  $\frac{N(X)}{N_H} = \frac{N(X)}{N(H)+2N(H_2)}$ , with  $N(H_2) \approx 3 \times 10^{22}$  cm<sup>-2</sup> and  $N(H) \approx 3 \times 10^{21}$  cm<sup>-2</sup> (Cuadrado et al. 2015, and references therein). (a) Rotational temperatures and column densities from rotational diagram analysis. (b)  $\Delta N$  calculated assuming an error of 15%. (c) Total column densities calculated as the sum of the *cis* and *trans* species.

the resulting rotational diagrams assuming extended emission. Table C.1 lists the  $T_{\text{rot}}$  and  $N$  obtained by linear least squares fits. The uncertainties shown in Table C.1 indicate the uncertainty obtained in the fit. The uncertainties obtained in the determination of the fit line parameters with CLASS are included in the error bars at each point of the rotational diagram.

To crosscheck that the relative intensities of the detected *cis*- and *trans*-HCOOH rotational lines are those expected according to their inferred rotational temperatures (i.e. that the assigned lines are not blended with lines from other molecules), we carried out a simple excitation and radiative transfer calculation using MADEX. We assumed that the *cis*- and *trans*-HCOOH rotational levels are populated following a Boltzmann distribution at a single rotational temperature (obtained from the rotational diagrams). For a given column density  $N$ , the model computes each line opacity (optically thin for the observed HCOOH lines) assuming a Gaussian line profile (for a linewidth of 2 km s<sup>-1</sup>) and simulates the output mm spectrum at a given spectral resolution. Figures 2 and D.1 show the observed spectra (black histograms) and the modelled lines (red curves) for the  $T_{\text{rot}}$  and  $N$  values obtained assuming extended emission. The good agreement of the fits, and lack of any other candidate line from a different molecule in our catalogue, confirms that all detected lines belong to *cis*- and *trans*-HCOOH.

## Appendix E: Non-detection of *cis*-HCOOH towards the Orion BN/KL hot core and Barnard-B1

We searched for *cis*-HCOOH in regions shielded from strong FUV radiation fields. We selected chemically rich sources for which we have also carried out deep mm-line surveys with the IRAM-30m telescope. In particular, we searched for HCOOH towards the hot core in Orion BN/KL (Tercero et al. 2010) and towards the quiescent dark cloud Barnard 1-b (B1-b; Cernicharo et al. 2012). Although we clearly detected lines from *trans*-HCOOH towards both sources, we did not find lines from *cis*-HCOOH above the detection limit of these deep surveys. Using the MADEX excitation code, we derived lower limits to the *trans*-to-*cis* abundance ratio towards these sources. Below we summarise the main results from these observations:

**Orion BN/KL hot core:** the hot core is embedded in the Becklin-Neugebauer/Kleinmann-Low massive star-forming region, at  $\sim 4'$  North-West from the Orion Bar, and  $\sim 0.5'$  North-West from the Trapezium stars. Relatively narrow lines ( $\Delta v_{\text{FWHM}} \approx 3$  km s<sup>-1</sup>) corresponding to *a*-type transitions of *trans*-HCOOH, with upper level energies up to  $E_u/k \approx 300$  K, are detected at a LSR velocity of  $\sim 8$  km s<sup>-1</sup>. The observed line parameters are consistent with emission from the hot core itself. This is dense,  $n_H$  of a few  $10^7$  cm<sup>-3</sup>, and hot gas at about 200 K

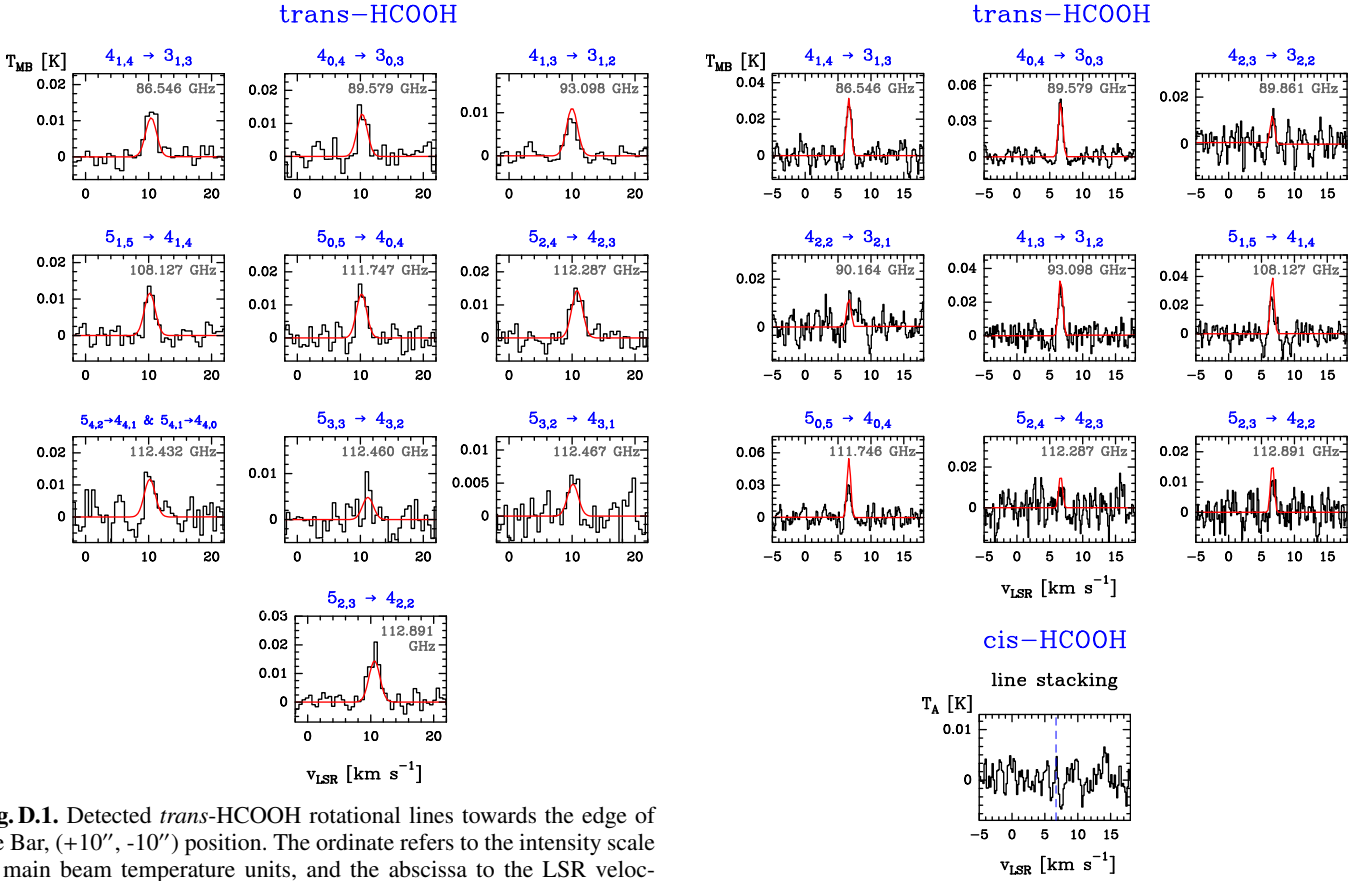


**Fig. D.1.** Detected *trans*-HCOOH rotational lines towards the edge of the Bar, (+10", -10") position. The ordinate refers to the intensity scale in main beam temperature units, and the abscissa to the LSR velocity. Line frequencies (in GHz) are indicated at the top-right of each panel together with the rotational quantum numbers (in blue). The red curve shows an excitation model that reproduces the observations. *Cis*-HCOOH lines are shown in Fig. 2.

**Fig. E.1.** Detected *trans*-HCOOH rotational lines towards the cold cloud Barnard 1-b. The ordinate refers to the intensity scale in main beam temperature units and the abscissa to the Doppler velocity. Line frequencies (in GHz) are indicated at the top of each panel together with the rotational quantum numbers. The red curve shows an excitation model that reproduces the rotational population diagram. The bottom panel shows the stacked spectra for *cis*-HCOOH.

(Blake et al. 1987; Tercero et al. 2010), and also from the more extended warm gas (about 60 K) in the ambient molecular cloud, so-called the extended ridge (Blake et al. 1987; Tercero et al. 2010). Using MADEX and our accumulated knowledge of the source structure (see Tercero et al. 2010; Cernicharo et al. 2016 and references therein), we determine  $T_{rot}(trans) = 100 \pm 35$  K and  $N(trans) = (1.0 - 0.3) \times 10^{15}$  cm<sup>-2</sup> in the hot core, and  $T_{rot}(trans) = 40 \pm 15$  K and  $N(trans) = (1.0 - 0.3) \times 10^{14}$  cm<sup>-2</sup> in the extended ridge. We note that the extended ridge is the main responsible for the observed *trans*-HCOOH line emission in the 3 mm band. Although we obtain much higher *trans*-HCOOH column densities compared to the Orion Bar, lines from *cis*-HCOOH are not detected towards the hot core. Assuming  $T_{rot}(trans) = T_{rot}(cis)$ , we compute a lower limit to the *trans*-to-*cis* abundance ratio of >100 in the hot core, and >30 in the extended ridge.

**B1-b cold cloud:** Barnard 1 is a low mass star-forming region located in the Perseus cloud. The cold core B1-b harbours two submillimetre continuum sources (B1-bN and B1-bS) identified as first hydrostatic core candidates (Gerin et al. 2015), and B1b-W, an infrared source detected with Spitzer (Jørgensen et al. 2006). Complex organic molecules such as CH<sub>3</sub>OCOH, CH<sub>3</sub>SH, and CH<sub>3</sub>O have been identified (Marcelino 2007; Öberg et al. 2010; Cernicharo et al. 2012). We detect nine lines from *trans*-HCOOH in the 3 mm band. A rotational diagram provides  $T_{rot}(trans) = 12 \pm 4$  K and  $N(trans) = (1.5 \pm 0.5) \times 10^{12}$  cm<sup>-2</sup>. Figure E.1 shows the

detected lines together with our best model fit (red curve). Lines are very narrow ( $\Delta v_{FWHM} \approx 0.5$  km s<sup>-1</sup>), consistent with emission from quiescent cold gas (about 20 K) shielded from FUV radiation. Although the inferred *trans*-HCOOH column density is similar to that obtained towards the Orion Bar, we do not detect lines from *cis*-HCOOH at the noise level of the B1-b data. Assuming  $T_{rot}(trans) = T_{rot}(cis)$ , we determine a lower limit to the *trans*-to-*cis* abundance ratio of >60. This is similar to that of the extended molecular Ridge of Orion, but significantly higher than towards the Bar.

**Appendix F: Detected *cis*- and *trans*-HCOOH lines  
towards the Orion Bar PDR**

**Table F.1.** Line parameters for *cis*-HCOOH towards the Orion Bar, (+10'', -10'') position.

Transition $(J_{K_a, K_c})_u \rightarrow (J_{K_a, K_c})_l$	Frequency [MHz]	$E_u$ [K]	$A_{ul}$ [s <sup>-1</sup> ]	$S_{ij}$	$g_u$	$\int T_{MB} dv$ [mK km s <sup>-1</sup> ]	$v_{LSR}$ [km s <sup>-1</sup> ]	$\Delta v$ [km s <sup>-1</sup> ]	$T_{MB}$ [mK]	S/N
4 <sub>1,3</sub> → 4 <sub>0,4</sub>	82740.491	14.5	2.32 × 10 <sup>-5</sup>	4.3	9	18.9(2.3)	10.5(0.2)	1.8(0.4)	8.7	4.7
4 <sub>1,4</sub> → 3 <sub>1,3</sub>	85042.744	13.8	2.10 × 10 <sup>-5</sup>	3.7	9	15.3(3.5)	10.6(0.3)	2.1(0.5)	6.6	3.5
5 <sub>1,4</sub> → 5 <sub>0,5</sub>	86556.490	19.9	2.59 × 10 <sup>-5</sup>	5.1	11	26.3(3.5)	10.0(0.2)	2.4(0.4)	10.1	5.6
4 <sub>0,4</sub> → 3 <sub>0,3</sub>	87694.689	10.5	2.45 × 10 <sup>-5</sup>	4.0	9	26.6(2.3)	10.6(0.1)	2.0(0.2)	12.7	9.6
4 <sub>1,3</sub> → 3 <sub>1,2</sub>	90661.090	14.5	2.54 × 10 <sup>-5</sup>	3.7	9	21.2(2.4)	10.3(0.1)	1.8(0.3)	11.2	4.8
7 <sub>0,7</sub> → 6 <sub>1,6</sub>	90910.082	29.4	1.50 × 10 <sup>-5</sup>	3.5	15	10.9(2.4)	10.1(0.2)	1.5(0.4)	6.9	3.9
6 <sub>1,5</sub> → 6 <sub>0,6</sub>	91291.549	26.5	2.95 × 10 <sup>-5</sup>	5.9	13	20.1(3.5)	10.3(0.2)	2.5(0.6)	7.5	5.7
7 <sub>1,6</sub> → 7 <sub>0,7</sub>	97025.449	34.1	3.42 × 10 <sup>-5</sup>	6.6	15	15.5(2.4)	10.5(0.1)	1.8(0.3)	7.0	4.4
8 <sub>1,7</sub> → 8 <sub>0,8</sub>	103845.157	42.8	4.02 × 10 <sup>-5</sup>	7.1	17	20.5(3.6)	10.0(0.2)	1.6(0.2)	12.2	5.2
5 <sub>1,5</sub> → 4 <sub>1,4</sub>	106266.589	18.9	4.28 × 10 <sup>-5</sup>	4.8	11	22.2(2.4)	10.7(0.1)	1.8(0.3)	11.0	4.5
5 <sub>0,5</sub> → 4 <sub>0,4</sub>	109470.705	15.8	4.87 × 10 <sup>-5</sup>	5.0	11	35.7(3.6)	10.3(0.1)	1.8(0.2)	18.6	7.1
5 <sub>1,4</sub> → 4 <sub>1,3</sub>	113286.704	19.9	5.19 × 10 <sup>-5</sup>	4.8	11	39.6(5.3)	10.7(0.2)	1.9(0.3)	19.7	6.0

**Table F.2.** Line parameters for *trans*-HCOOH towards the Orion Bar, (+10'', -10'') position.

Transition $(J_{K_a, K_c})_u \rightarrow (J_{K_a, K_c})_l$	Frequency [MHz]	$E_u$ [K]	$A_{ul}$ [s <sup>-1</sup> ]	$S_{ij}$	$g_u$	$\int T_{MB} dv$ [mK km s <sup>-1</sup> ]	$v_{LSR}$ [km s <sup>-1</sup> ]	$\Delta v$ [km s <sup>-1</sup> ]	$T_{MB}$ [mK]	S/N
4 <sub>1,4</sub> → 3 <sub>1,3</sub>	86546.180	13.6	6.35 × 10 <sup>-6</sup>	3.7	9	23.8(3.5)	10.4(0.1)	1.8(0.3)	13.7	7.0
4 <sub>0,4</sub> → 3 <sub>0,3</sub>	89579.168	10.8	7.51 × 10 <sup>-6</sup>	4.0	9	27.9(4.7)	10.3(0.1)	1.8(0.2)	14.9	5.3
4 <sub>2,3</sub> → 3 <sub>2,2</sub>	89861.473	23.5	5.69 × 10 <sup>-6</sup>	3.0	9	26.4(7.0)	10.0(0.4)	2.2(0.7)	11.3	3.0
4 <sub>1,3</sub> → 3 <sub>1,2</sub>	93098.350	14.4	7.91 × 10 <sup>-6</sup>	3.7	9	26.3(2.4)	10.0(0.1)	2.2(0.2)	9.9	6.2
5 <sub>1,5</sub> → 4 <sub>1,4</sub>	108126.709	18.8	1.30 × 10 <sup>-5</sup>	4.8	11	28.7(2.4)	10.2(0.1)	1.5(0.2)	14.0	8.3
5 <sub>0,5</sub> → 4 <sub>0,4</sub>	111746.771	16.1	1.49 × 10 <sup>-5</sup>	5.0	11	27.9(3.6)	10.2(0.1)	1.7(0.3)	16.2	5.2
5 <sub>2,4</sub> → 4 <sub>2,3</sub>	112287.131	28.9	1.27 × 10 <sup>-5</sup>	4.2	11	32.2(3.6)	10.7(0.1)	2.1(0.2)	14.2	6.1
5 <sub>3,3</sub> → 4 <sub>3,2</sub>	112459.608	44.8	9.73 × 10 <sup>-6</sup>	3.2	11	9.1(3.6)	11.2(0.1)	0.5(0.4)	16.5	5.2
5 <sub>3,2</sub> → 4 <sub>3,1</sub>	112466.993	44.8	9.73 × 10 <sup>-6</sup>	3.2	11	14.0(3.6)	10.1(0.3)	1.8(0.5)	7.3	2.8
5 <sub>4,2</sub> → 4 <sub>4,1</sub>	112432.278	67.1	5.47 × 10 <sup>-6</sup>	1.8	11	} 24.9(6.1)	10.2(0.2)	1.6(0.4)	14.4	3.1
5 <sub>4,1</sub> → 4 <sub>4,0</sub>	112432.305	67.1	5.47 × 10 <sup>-6</sup>	1.8	11					
5 <sub>2,3</sub> → 4 <sub>2,2</sub>	112891.429	28.9	1.29 × 10 <sup>-5</sup>	4.2	11	29.2(3.6)	10.6(0.1)	2.0(0.2)	17.6	7.3